Generation of upper trailing counter rotating vortices of transverse sonic jet in a supersonic crossflow at Ma=2.7

M.B. Sun[1*], Z.W. Hu[2]

[1]Science and Technology on Scramjet Laboratory, National University of Defense Technology, Changsha, 410073, China

[2]Faculty of Engineering and the Environment, University of Southampton, Southampton, SO17 1BJ, UK

E-mail: wind_flowcfd@163.com; sunmingbo@nudt.edu.cn

Abstract: Direct numerical simulations were conducted to investigate physical structures of a transverse sonic air jet injected into a supersonic air crossflow at a Mach number of 2.7. Simulations were run for two different jet-to-crossflow momentum flux ratios (*J*) of 1.85 and 5.5. The main averaged flow features around the transverse jet, such as major counter rotating vortices (CRVs) and trailing CRVs (TCRVs) were captured. The major CRVs form in the lateral portion of the jet plume and absorb other induced trailing vortices downstream of the jet plume. Upper trailing CRVs form above the major CRVs downstream of the jet barrel shock. The streamline analysis indicates that the upper trailing CRVs are related to the Mach disk. As the streamlines penetrate the lateral side of Mach disk where a strong shear condition exists, the baroclinic torque induces upper vorticities in the opposite rotating direction against the major CRVs. Downstream of the Mach disk, the baroclinic vorticity production along the streamlines tends to approach zero, which means no more torque is pumped into the farfield and the upper TCRVs are merged into the major CRVs by their suction.

Keywords: supersonic flow; transverse jet; direct numerical simulation; counter rotating vortices;

upper trailing counter rotating vortices

Nomenclature

J =jet-to-crossflow momentum flux ratio

BVP = baroclinic vorticity production

CRV = counter rotating vortices

DNS =direct numerical simulation

JISC =jet interaction with supersonic crossflow

LES =large eddy simulation

STBL =supersonic turbulent boundary layer

TCRV =trailing counter rotating vortices

1. Introduction

A sonic jet in supersonic crossflow is one of the most fundamental canonical flows for the investigation of turbulent mixing and combustion at both the fundamental and the applied level in scramjet engine combustors. It is of relative simplicity, yet it maintains many features of interest, such as three-dimensionality, shock structures, separation and recirculation, wall-bounded effects and jet wakes. A significant body of work has been conducted to characterize and study this system. Two recent review articles on the study of transverse jets are written by Karagozian (2010)[1] and Mahesh (2013)[2].

A typical configuration of the transverse jet by under-expanded sonic injection into a supersonic crossflow from a wall surface is illustrated in Fig. 1a).[3, 4] The upstream recirculation, the bow shock and recovery of the downstream separation have been described in details previously.

The under-expanded jet expands through a Prandtl–Meyer fan at the lip of the jet orifice before the jet flow is compressed by the barrel shock and the Mach disk. The jet forms a pair of counter-rotating vortices whose axis is aligned with the downstream direction. The far field is dominated by a major counter-rotating vortex pair (CRV). Lower trailing CRVs are generated on the wall surface due to the low-pressure recirculation zone in the jet leeside and the suction action of the major CRVs. Viti et al.[5] gave a schematic of the cross flow section at a location aft of the barrel shock to demonstrate the different pairs of trailing CRVs, as shown Fig.1b). The kidney-shaped CRVs form downstream of the jet plume and are the major contributors to the mixing of the injectant with the freestream. The lower trailing vortex remains attached to the solid surface as it entrains fluid from the surrounding boundary layer. The trailing upper vortex is weaker than the other vorticities hence more difficult to identify.

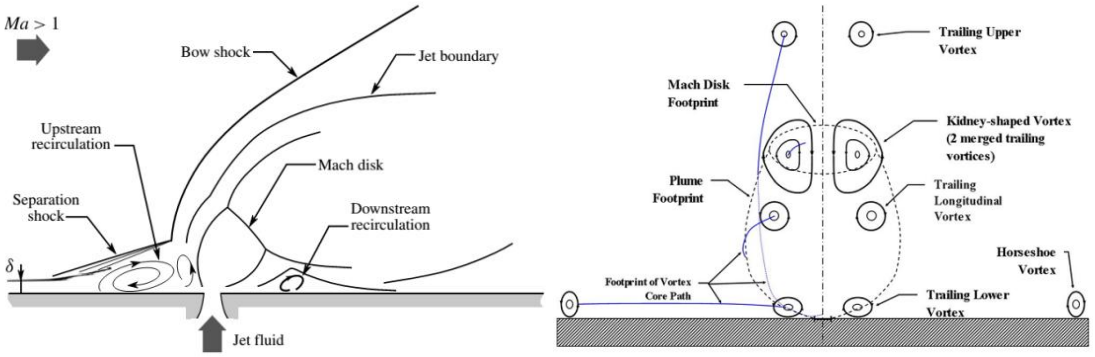

Fig.1 Schematic diagrams of a sonic transverse jet in supersonic crossflow showing some of the dominant flow features: (a) side-view; (b) flow field at a transverse section aft of the barrel shock

Numerous experimental investigations have been conducted to understand the mechanisms of the jet injection into a supersonic crossflow, which include detailed velocity measurements[6], time-averaged wall-pressure measurements[7], penetration height[8], temporally resolved flow visualizations[9, 10] and mixing characteristics[3] with nonreactive and combustible gaseous jets[4]. These measurements show the overall jet flow features and the dynamics of the jet shear layer and

shocks along with extended flow data that can be used as validation data for numerical predictions. Because of the difficulty in measuring the high-speed complex unsteady flowfields, experimental data are mainly obtained for certain transverse and longitudinal 2-D slices of the flowfield.

Recently a number of numerical simulations have been conducted and the detailed flowfield and coherent structure behavior have been obtained. Kawai et al.[11] and Rana et al.[12] performed large eddy simulations (LES) of sonic jets in a supersonic stream and their results demonstrated Kelvin-Helmholtz (K-H) instabilities in the interface of the jet shear layer confronted with the main airstream. Won et al. [13] used detached-eddy simulation (DES) to reveal vortex evolvement under the jet conditions of Ben-Yakar's experiment[3]. Chai et al. [14] conducted LES on the flowfield of sonic jets in supersonic crossflow and the trajectory of the transverse jet was investigated. In our previous work[15, 16], hybrid RANS/LES methods were validated and conducted to study three-dimensional jet mixing and the effect of microramps on jet mixing in supersonic crossflow. When combined, the experimental results and numerical simulations have well revealed the shock structures and the jet vortices resulting from a sonic transverse jet injecting into a supersonic crossflow. The mechanism on formation of major CRVs has also been well explained. Here we will focus on the trailing CRVs. Viti et al.[5] discussed the details of the upper and lower trailing CRVs at a cross flow of Ma=4.0. The trailing lower CRVs on the wall surface were induced due to the recirculation zone on the jet leeward side. Upper TCRVs on top of the major CRVs were captured. Rana et al.[12] simulated the jet interaction with Mach 1.6 supersonic crossflow and did not observe this phenomenon. They concluded that the major CRVs are a common feature but the upper TCRVs depend upon the free-stream Mach number. Kawai and Lele[11] simulated the same case as Rana et al. [12] on a finer grid and observed the weak upper trailing vorticities. Viti et al. [5] found there are

three pairs of trailing CRVs which finally merge into the kidney-shaped major CRVs. They gave qualitative analysis on the formation of three pairs of the TCRVs. There are no corresponding experiments to demonstrate this topic currently.

In the present study, direct numerical simulation (DNS) is conducted to investigate sonic jet in a supersonic crossflow at Ma=2.7. This work aims at producing a detailed physical analysis of trailing CRVs in the jet interaction with supersonic crossflow (JISC) field. Such an analysis can improve the understanding of the relevant flow structures responsible for the mixing of the injectant with the cross flow. This paper is organized as follows. The algorithm, the simulation conditions, description of the computational grid, turbulent inflow generator and the validation are discussed in Section 2. A brief description of the instantaneous jet flowfield is presented in Section 3.1.The mean flowfield of the trailing CRVs is presented in Section 3.2 and the three-dimensional streamlines are given to exhibit different types of trailing CRVs. Section 3.3 mainly discusses the upper trailing CRVs and their generation mechanism related to baroclinic effects.

2. Flow conditions and numerical setup

2.1 Numerical simulation and inflow condition

All simulations in this paper solve the three-dimensional unsteady compressible Navier-Stokes equations directly without any modeling, using an in-house DNS code. The code has been developed over a number of years and applied to studies of instability, transition and turbulence in high-speed flows (Sandham et al, 2014).[17] Here we provide the main features of the code and explain the run conditions for the present study. The detailed governing equations of continuity, momentum, total energy for three-dimensional flowfield are omitted for brevity.

The air inflow parameters (shown in Table 1) are set in accordance with the *Ma*=2.7

experiments of Sun et al. (2013)[10] with stagnation pressure P_0 = 101325 Pa, stagnation temperature T_0=300 K. The bottom wall 99% boundary-layer thickness, which is the same for all simulations, is estimated to be δ_i=5.12 mm, with the compressible (including density variations) boundary-layer displacement and momentum thicknesses δ_i^*=1.75 mm, θ=0.38 mm and Reynolds numbers $Re_{\delta*}$=15,367, Re_θ=3,337. A sketch of the computational domain is shown in Fig.2.

Two momentum flux ratios J=1.85 and J=5.5 of air injection are used. Both cases lead to a sonic jet with stagnation temperature T_{0i}=300 K. The jet properties are set to correspond to the injection parameter as shown in Table 2. Since the turbulent levels originating from the jet orifice are not known, a uniform profile across the jet orifice is implemented without disturbance. It might be argued that turbulence would not be thoroughly resolved in the jet; however, it is believed that the jet behavior and macro flow topology will not be affected by this assumption.

Table 1. Air flow conditions for the simulations, including the dimensional boundary-layer (BL) thicknesses and Reynolds number at the inflow

Mach number	Stagnation temperature	Stagnation pressure	BL 99% thickness	Momentum thickness	Reynolds number
Ma_∞	T_0	P_0	δ_i	Θ	Re_θ
2.7	300 K	101 kPa	5.12mm	0.38mm	3337

Table 2. Jet conditions for the simulations

Air jet-to-crossflow momentum flux ratio	Mach number	Jet orifice diameter	Stagnation temperature	Stagnation pressure
J	M_j	D	T_{0j}	P_{0j}
1.85	1.0	2 mm	300 K	110 kPa
5.5	1.0	2 mm	300 K	330 kPa

2.2 Domain and grid distribution

Although the use of a digital filter to generate the inflow boundary condition significantly reduces the length required for boundary-layer development (Xie and Castro),[18] there should nevertheless be enough distance to allow the boundary layers to adjust to an equilibrium state upstream of the jet. It was found that a distance of 12 times the inflow boundary-layer thickness is enough to obtain realistic turbulent mean and RMS profiles from the digital filter inflow generator used. Accordingly, the initial length is set to be $L_i \approx 13\delta_i \approx 65$mm for a fully developed turbulence generation (the region is denoted as STBL, supersonic turbulent boundary layer). The jet plume length is given to be L_m=90mm including nearfield (denoted as JISC section1) with 10 mm upstream and 40 mm downstream of the jet and farfield (denoted as JISC section2) of 40 mm. Therefore, the total length of the physical domain is L_x=155mm. The wall-normal extent of the domain is 18 mm, and a span of 14 mm is used. The jet is centred 75mm downstream of the inlet with an orifice diameter of D=2mm.

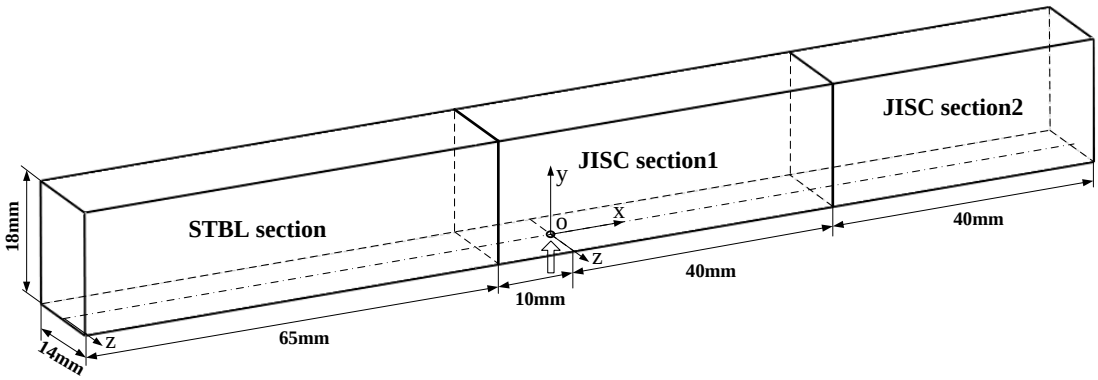

Fig. 2 Schematic domain of the domain selected for the STBL (supersonic turbulent boundary layer) and JISC (jet interaction with a supersonic crossflow) simulations. An arrow points to the jet orifice position.

Fig. 2 shows the geometry of the physical domain (without the buffer layers), which is 155 mm, 18 mm, 14 mm in the streamwise (x), wall-normal (y) and spanwise (z) directions, respectively,

for a Cartesian coordinate system with origin at the jet centre, which is 75mm downstream of the inlet. A fine grid of 2305×279×271 grid points is used for the current simulations, as shown in Fig.3 for the two-dimensional *x-y* grid, plotted every nine and four points in the streamwise and wall-normal directions, respectively. In the streamwise direction, a uniform grid is adopted to capture the boundary layer flow characteristics for x≤-10mm, which is linked smoothly by stretching grids within -10mm<x≤-5mm to a refined uniform grid for -5mm<x≤40mm in the JISC section1 to capture the structures in the nearfield of the jet. In JISC section 2, the grid is first stretched within 40mm<x≤45mm to a uniform grid for the farfield region 45mm<x≤80mm, where the grid has the same resolution as used in the STBL section. In the wall-normal direction, the grid is clustered near the wall in the region y=0 to $0.6\delta_i$ uniformly and then stretched smoothly further out. A uniform grid is used in the spanwise direction.

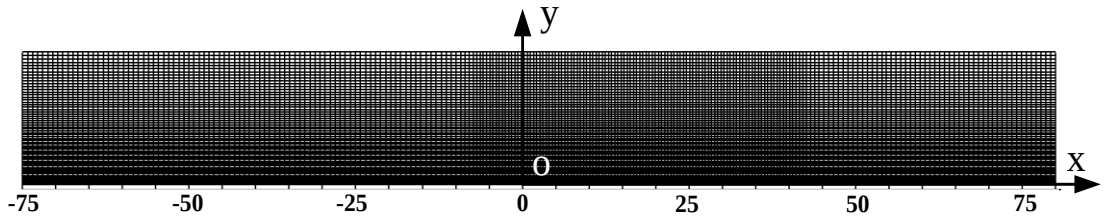

Fig. 3 The two-dimensional grid used for the simulations, plotted every nine points in the x direction point and every four points in the y direction.

Table 3 Computation grids for mesh of JISC and STBL domain

	N_x	N_y	N_z	Total (million)	Δ_x^+	Δ_y^+	Δ_z^+
JISC section1	945	279	271	74.5	4.1-6.6	0.8-10.0	4.1
JISC section2	516	279	271	39.0	6.6	0.8-10.0	4.1
STBL section	774	279	271	58.5	6.6	0.8-10.0	4.1

Large buffer layers (not shown in Figs. 2 and 3) with non-reflective outside-boundary set are

introduced with lengths of 15 mm, 11 mm and 12mm at the outlet, on both the lateral sides and the upper boundaries. The grid is smoothly stretched in the buffer layers toward the boundaries. The buffer layers with coarsened mesh help to damp fluctuations and minimize reflection from the boundaries.

Table 3 summarizes the number of grid points and resolutions in wall units, which are calculated based on the friction velocity of the incoming turbulent boundary layer at x=-15mm. In the wall-normal direction, the grid has y_1^+ =0.8 for the first point off the wall and Δy^+ =5.2 at the edge of the boundary layer and $\Delta y^+_{\max}$ =10.0 near to top boundary, as listed in Table 3. The fine mesh ensures good resolution of the near-wall turbulence. Since it is not known for the smallest turbulence scales in the jet field, the grid resolution of $\Delta y^+ \le 10.0$ would ensure the mainstream simulations as quasi-DNS (QDNS), as denoted by Sandham et al.[19] The uniform grids in STBL and JISC2 have Δx^+=6.6, while JISC1 has a resolution of Δx^+=4.1. In the spanwise direction, the grid is uniform with spacing fixed to Δz^+=4.1. The grid suitability for the present simulations was verified by coarsening the grid in all directions. The most sensitive feature was found to be the wall skin friction which varied by less than 5.6% at x=0mm, for a grid that was coarsened by 50% in all directions.

No-slip and adiabatic boundary conditions were enforced on the bottom wall (shown in figure 2). An integrated characteristic boundary condition was applied at the inflow, and an outflow condition with an integrated characteristic scheme was applied in the spanwise boundary, top boundary and exit boundary. The jet orifice is defined directly in the surface wall uniform grid and set to J=1.85 and J=5.5 with a sonic condition.

2.3 Numerical methods and validation

The governing equations are solved by using a high-order finite-difference code[20]. This code uses a fourth-order central difference scheme for the spatial derivatives and a third-order explicit Runge-Kutta scheme for time advancement. The code makes use of an entropy splitting of the Euler terms and the Laplacian formulation of the viscous terms to improve the stability of the non-dissipative central scheme. In addition, a variant of the standard total variation diminishing scheme is used for shock capturing[21]. To better resolve the steep gradient in flowfield around the injected jet, a hybrid scheme combining the entropy splitting central scheme with a fourth order central-upwind weighted essentially non-oscillation (WENO-CU4) scheme is used following the establishing procedure of the WENO-CU6[22], with details given in Appendix I. The two schemes are combined using the Ducros sensor[23] as the hybrid function. The numerical flux in the hybrid code consists of the linear combination of a non-dissipative central term and a shock capturing term,

$$\tilde{f}_{i+1/2} = \tilde{f}^{(e)}_{i+1/2} + \chi_{i+1/2}\left(\tilde{f}^{(w)}_{i+1/2} - \tilde{f}^{(e)}_{i+1/2}\right)$$

where the superscripts *e* and *w* denote quantities calculated by the entropy splitting central and the WENO schemes, respectively. The switching function is based on a dilatation/vorticity (θ/ω) sensor similar to that of Ducros et al.[23] $\chi = \dfrac{\theta^2}{\theta^2 + \omega_j\omega_j + \varepsilon}$. This is done for neighboring points to ensure that central differencing is not applied across any shocks.

The digital filter inflow generation method of Xie and Castro[18] is used to generate a more realistic supersonic turbulent boundary layer at the inflow. A detailed description of the optimized digital filter used here can be found in Touber's thesis[24]. The digital filter is robust to the choice of length scale, as long as the prescribed length scales are at least as large as the integral length scales of the real flow and sufficient downstream distance is provided to allow for the turbulence to develop[25]. In the present study, the streamwise characteristic length scales for the three velocity

components u, v and w are set to $0.65\delta_i$, $0.35\delta_i$ and $0.35\delta_i$ (where δ_i notes the 99% boundary-layer thickness at the inflow) respectively. The mean inflow profile is generated using the same approach of Touber and Sandham[26] beforehand. The inflow RMS values are taken from the DNS results of Schlatter and Orlu[27] for a similar Reynolds number.

Fig.4 shows the iso-surface of compressible Q-criterion on the flat plate upstream of the jet orifice colored by the local wall-normal distance, which is a vortex-identification scheme for compressible flow[28], i.e., $Q_c = \left(\|\mathbf{\Omega}\| - \|\mathbf{S}_D\|\right)/2$ ($\|\mathbf{G}\| = \sqrt{tr\left(\mathbf{G}\mathbf{G}^T\right)}$), where $\Omega_{ij} = 1/2\left(\partial u_i/\partial x_j - \partial u_j/\partial x_i\right)$ and $S_{D,ij} = 1/2\left(\partial u_i/\partial x_j + \partial u_j/\partial x_i\right) - 1/3\left(\partial u_k/\partial x_k\right)\delta_{ij}$ [29, 28]. The results demonstrate that details of the boundary layer development are clearly captured. The boundary layer upstream of the jet orifice has gone into a sufficiently developed turbulent mode.

Statistical data are based on averaging flowfields over 100 non-dimensional time units (D/U_∞) after running the simulations for 200 non-dimensional units to let the flow develop. Turbulent boundary-layer mean profiles and distributions of RMS values at 60mm downstream of the inlet are first evaluated, as shown in Fig. 5. Since the coordinate origin is at the jet center, which is 75mm downstream of the inlet, the position 60mm downstream of the inlet corresponds to x=-15mm (x/D=-7.5). [26][27]A compressible scaling, suggested by Morkovin[29] and validated by Duan et al.[30] for high Mach numbers, is used to transform the incompressible RMS values. The boundary layer thickness at x/D=-7.5 is $\delta_0 \approx 5.65$mm and the compressible boundary-layer displacement and momentum thicknesses is δ_i^*=2.12mm, θ=0.41mm respectively. It should be noted that the Reynolds number based on the freestream flow properties and the momentum thickness, i.e. $\mathrm{Re}_\theta = \rho_e U_e \theta/\mu_w$ is 3,600. The corresponding Reynolds number under the van Driest scaling, i.e. $\mathrm{Re}_{\theta,vd} = \rho_w U_e^{vd} \theta^{vd}/\mu_w$, is 917, which is close to the Reynolds number of 1000 in the incompressible

case of Schlatter and Orlu[27]. The subscripts '*e*' and '*w*' above denote the main flow and inner parameters parameter, while the superscript '*vd*' means the value under the van Driest transform. In zero pressure gradient, Van Driest transformation is expected to reproduce the log-law[31] of the wall as in incompressible turbulent boundary layers, which is valid in Fig.5. Morkovin[29] predicted that scaling by the square root of the mean density profile should collapse RMS data for the streamwise velocity component and possibly the spanwise and wall-normal components. The calculated non-dimensional freestream velocity is seen to be slightly higher, which is caused by an underestimation of the skin friction. The RMS values collapse well with the DNS results of Schlatter and Orlu[27], which indicates that the digital filter inflow generation method used here is effective.

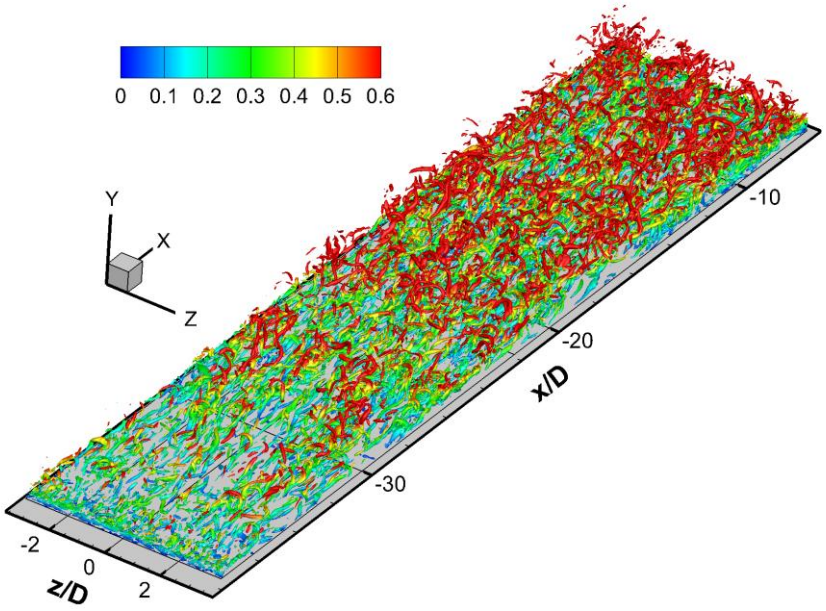

Fig. 4 Iso-surface of compressible *Q*-criterion (*Q* =0.6, non-dimensionalized by freestream velocity and jet orifice diameter) fields of the incoming boundary layer colored by the wall normal distance

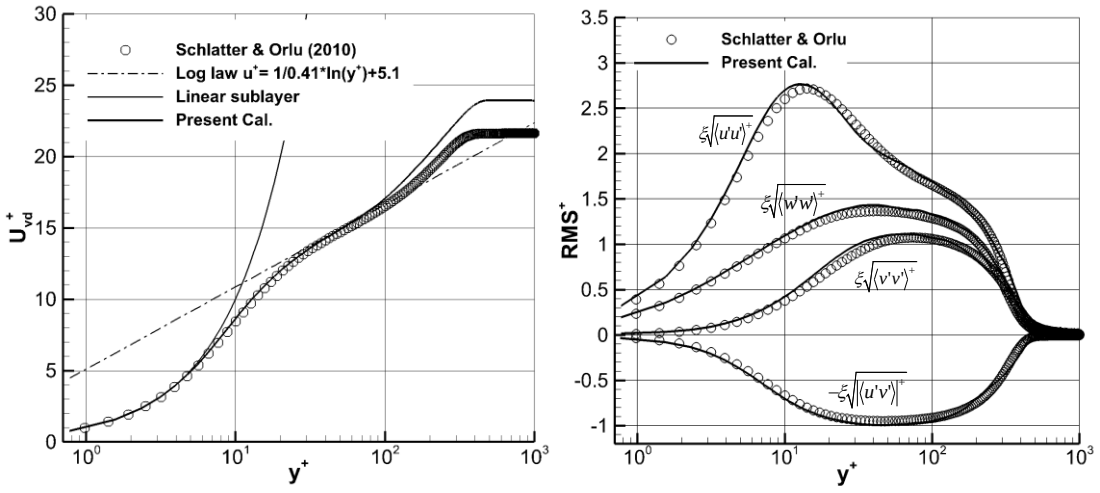

a) Mean velocity distribution b) RMS velocity distribution

Fig. 5 Mean and RMS velocity distributions obtained at 60 mm downstream of the inlet. The van Driest transformation was applied to the mean velocity and a compressible scaling $\xi = \sqrt{\rho/\rho_w}$ to the RMS curves.

3. Numerical results and analysis

All simulations were performed on Archer, UK National Supercomputer. Each simulation requires approximately 180,000 PE hours to collect statistics over 100 non-dimensional time units (D/U_∞).

3.1 Instantaneous flow structures

Typical instantaneous simulated results of density contours in the flowfield of J=1.85 and J=5.5 are shown in Fig. 6. The results reveal detailed structures of the unsteady jet penetration. In particular the bow shock, barrel shock, Mach disk and separation bubbles are well-identified. The upstream separation shock is not as strong as the other shocks. The turbulent structures are developed in the upstream boundary layer and impinge with the jet. Large scale structures originate from the windward interface of the jet with the air stream and develops along the streamwise direction. It is known that the vortical behavior in the near-field is very important and determines

the scale of eddies in the far-field[10]. Analysis of the jet structure can be found in previous literatures, therefore is not detailed here. Typical instantaneous simulated results of streamwise vorticity iso-surface in the jet flowfield are shown in Fig.7. The vortical structures around the jet break down to well-developed turbulent eddies downstream. Sonic jet with higher *J* has a more intense interaction with the incoming flow and larger separation region and penetration height could be identified in these figures. The detailed analysis on jet structures is omitted here since many literatures have done that. We will focus on the trailing vortices in the vicinity of the jet. The instantaneous streamwise vorticity iso-surfaces seems quite complex and it is difficult to demonstrate the vortical behavior directly. Time-averaged flowfield will be used to give detailed analysis.

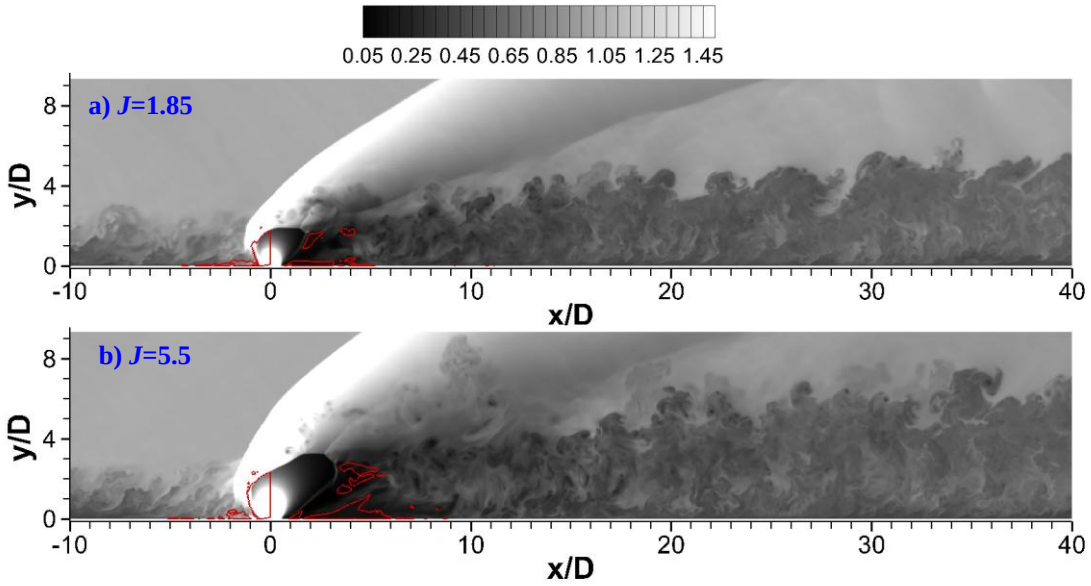

Fig. 6 Temperature contour at *z/D*=0.0 slice of jet interaction with supersonic crossflow. Isoline of u/U_∞=0.0 is superimposed in red color.

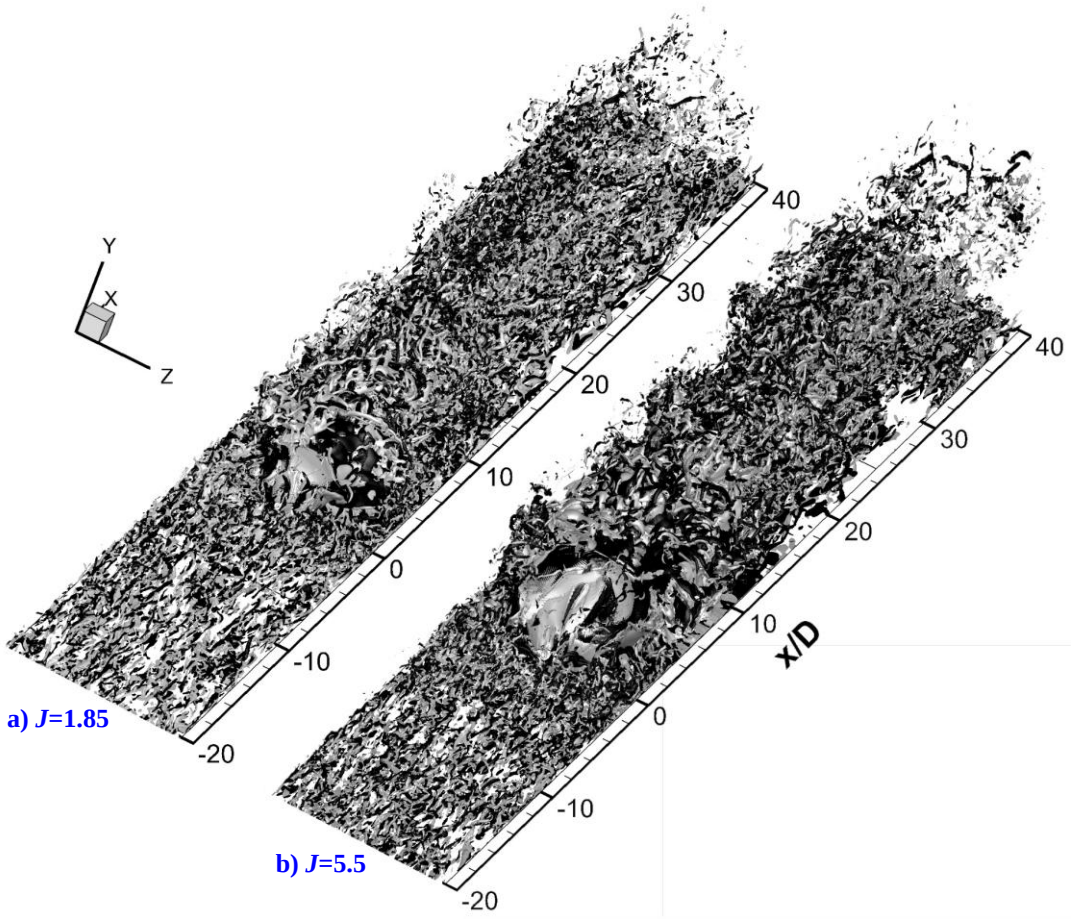

Fig. 7 Instantaneous iso-surfaces of streamwise vorticity iso-surface structures (Ω_x=-4 and 4, non-dimensionalized by freestream velocity and jet orifice diameter) of J=1.85 and J=5.5

3.2 Mean flow properties in the jet flowfield

Time averaged analysis is presented for flow visualization in Fig. 8 showing the contours of streamwise vorticity at different x-locations for J=1.85 and J=5.5. It is seen that in the vicinity downstream of the jet, there are several pairs of TCRVs around the major CRVs in Fig. 8a) and Fig. 8d). The upper and lower TCRVs rotate in an opposite direction against major CRVs. The lower surface TCRVs mainly are attached on the wall surface and some induced counter rotating vortices exist in the region between the major CRVs and the lower TCRVs. Those induced TCRVs develop and merge into the pair of the major CRVs in the downstream, as shown in Fig. 8b)-c) and Fig. 8 d)-e). The major CRVs grow in size but decrease in magnitude. The definition of upper TCRVs here

is not the same as that denoted by Viti et al.[5]. The upper TCRVs in this paper are similar to Trailing vortex 1 mentioned by Viti et al. [5]. The pair of upper TCRVs defined by Viti et al. could be indicated as top TCRVs in this study. The magnitude of top TCRVs is very weak and could not be well recognized in Fig.8 a) and d). Viti et al. gave a slice of vorticity magnitude of trailing vortex 2 and did not show the rotating direction. The generation of the upper TCRVs and the detailed flow topology in three dimensionality was not unveiled. It is not clear how the opposite rotation is energized. The lower TCRVs have been discussed a lot in previous studies and usually thought to be due to the low-pressure recirculation zone and the effects of the major CRVs. We will focus on the upper TCRVs and discuss the details.

To clearly demonstrate the CRVs, three-dimensional iso-surfaces of streamwise vorticity is shown in Fig. 9 for J=1.85 and J=5.5 respectively. In these figures, arrows with solid line point to major CRVs and arrows with dashed line point to upper TCRVs. It is identified that the upper TCRVs are located above the major CRVs. For J=1.85, the upper TCRVs extend only in a very short streamwise distance, which means that the pair of upper TCRVs are a common feature but depend upon J. Higher J leads to a more apparent upper TCRV phenomenon. It is concluded that the upper TCRVs have an opposite rotating direction against the major CRVs. As the jet plume evolves, the upper TCRVs disappear and only major CRVs exist in the farfield, which reflects a merging process in the downstream region.

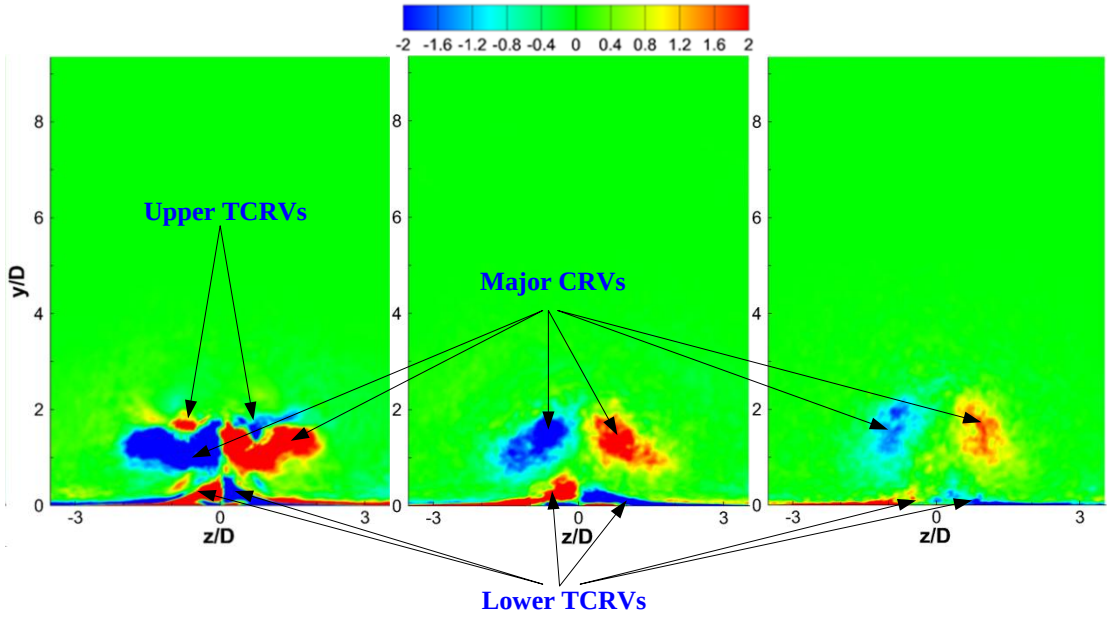

a) J=1.85, x/D=3 b) J=1.85, x/D=6 c) J=1.85, x/D=9

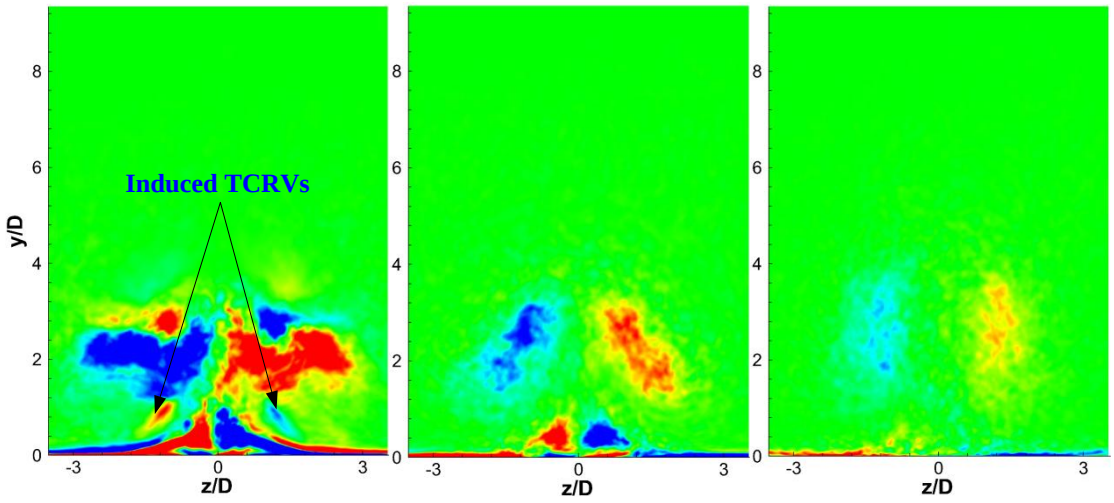

d) J=5.5, x/D=6 e) J=5.5, x/D=12 f) J=5.5, x/D=18

Fig. 8 Time averaged streamwise vorticity contours at streamwise slices at different axial locations for J=1.85 and 5.5, respectively

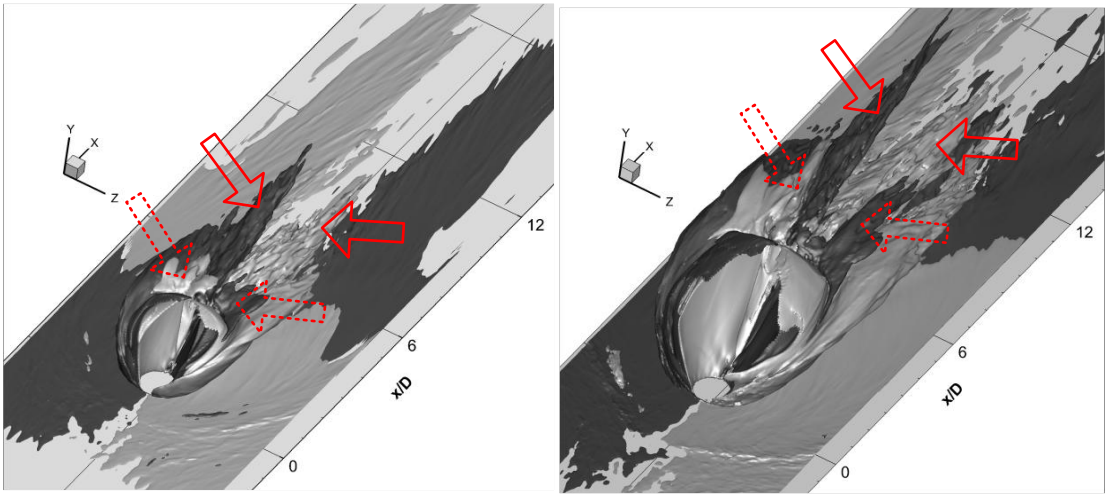

a) J=1.85 b)J=5.5

Fig. 9 Iso-surfaces of time averaged streamwise vorticity (Ω_x) for J=1.85 and 5.5 respectively, dark iso-surface corresponds to Ω_x=-2.0, gray iso-surface corresponds to Ω_x =2.0, non-dimensionalized by freestream velocity and characteristic length (D). Solid-line arrows point to major CRVs and dashed-line arrows point to upper TCRVs

Time averaged contours of Mach number on the z/D=0 slice with streamlines are shown in Fig.10a)-b) for J=1.85 and J=5.5. The bow shock and barrel shock are clear in these figures. The solid-line arrow points to the Mach disk. The three dimensional barrel shock and Mach disk are shown in Fig.10c) for J=5.5. The effect of the pressure difference between the jet windward and the leeward promotes the side flow and leads to a finlike structure on the lateral side of the barrel shock iso-surface of Mach number 3.1, which was also analyzed by Viti et al. [5] Transparent slice of z/D=-1.0 contoured with Mach number is also shown in Fig.10c). Slice of z/D=-1.0 corresponds to central location of the upper TCRV shown in Fig.8d). As shown in Fig.10c), behind the Mach disk, flow is recompressed to a lower Mach number and the slow-moving injectant fluid comes in contact with the high-speed cross flow fluid aft of the Mach disk.

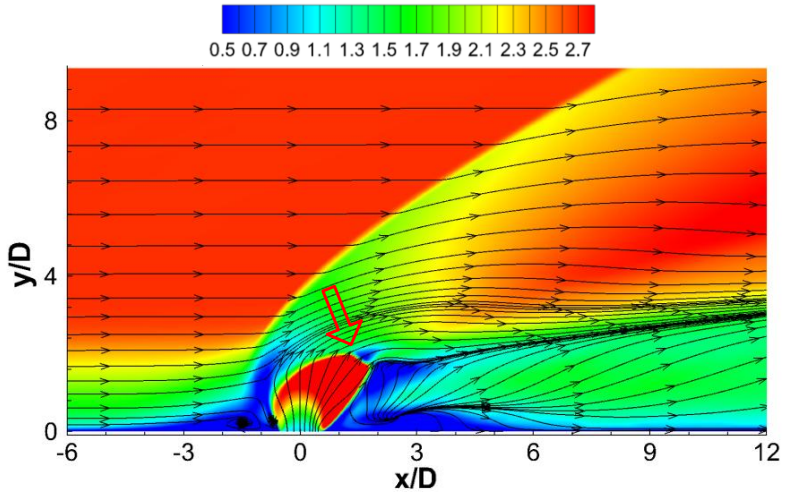

a) J=1.85, slice of z/D=0.0 and arrow points to Mach disk

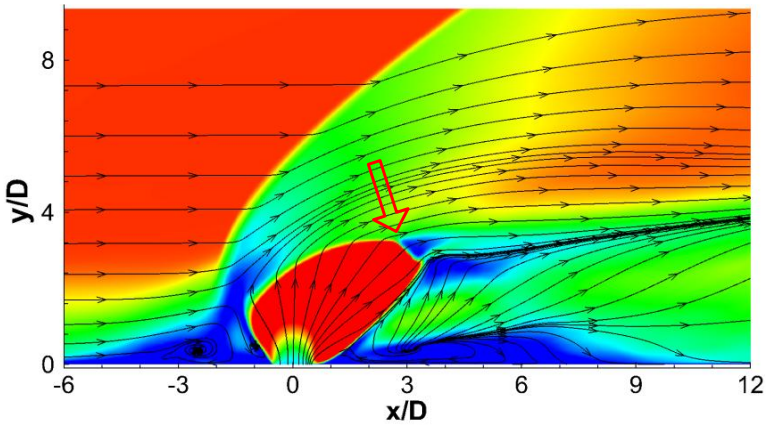

b) J=5.5, slice of z/D=0.0 and arrow points to Mach disk, same legend with a)

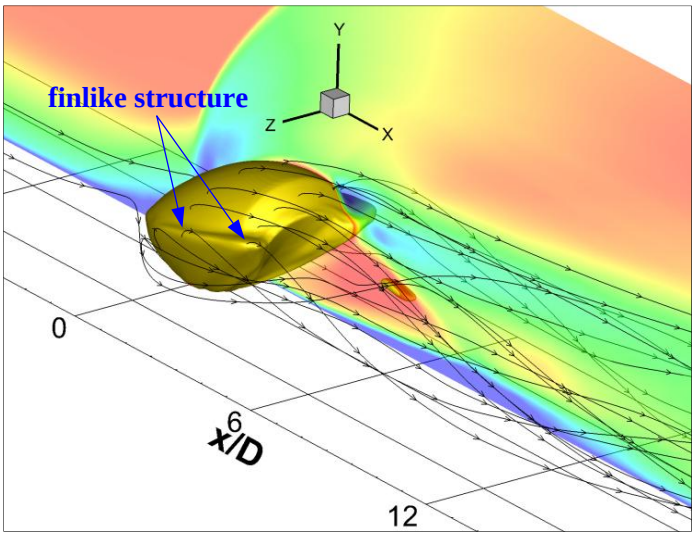

c) J=5.5, iso-surface of the barrel shock (Ma=3.1) and z/D=-1.0 slice, same legend with a)

Fig. 10 Time averaged contours and iso-surface of Mach number of J=1.85 and 5.5.

Stream ribbons colored by local streamwise vorticity are given in Fig.11 to demonstrate the trailing CRVs in the jet plume. Stream ribbons roll along different directions, which reflect the local vorticity. In Fig.11a)-b), the ribbons exhibit that upper TCRVs are related to the Mach disk formed in the expanded jet plume. Black arrows shown in Fig.11a) indicate the lateral rolling direction. As the stream ribbons penetrate the lateral side of the Mach disk, the stream gets energized and acquires enough torque from the local shear field to twist. This twisting corresponds to the generation of the upper trailing vortex. In the region near to the centerline plane, the ribbons are not obviously twisted, which demonstrates that there is no strong torque generation in the centerline plane of the Mach disk. The major CRVs originate from the lateral shear layer between the barrel shock and the freestream, as shown in Fig.11c). The stream ribbons come from the lateral side of the injector and twist when going around the jet barrel shock. Part of the ribbons come from the crossflow and are entrained to the edge of the major CRV region. It is inferred that as the barrel shock detaches from the wall surface, it creates the low-pressure region which absorbs the lateral flow. As shown in Fig. 11a)-c), the stream ribbons of the upper TCRVs and major CRVs bind together into a rope-like structure in the farfield, which represents that they merge into a single vortex as they trail downstream. These ribbons twist and roll around a vortex core in a common longitudinal axis, which corresponds to the major merged vorticity shown in Fig.8f) and Fig.9b). Fig.11c) demonstrates the lower TCRVs and the induced TCRVs located between the major CRVs and the lower TCRVs. Ribbons of the lower surface TCRVs move across the separation bubble and run into the low-pressure region behind the jet. The magnitude of rotation of the ribbons is very large since a highly twisted structure exists in the ribbons. The ribbons of the induced TCRVs originate from the crossflow near to the symmetric plane and they gain strength as they are convected downstream of

the lateral side of the barrel shock plume.

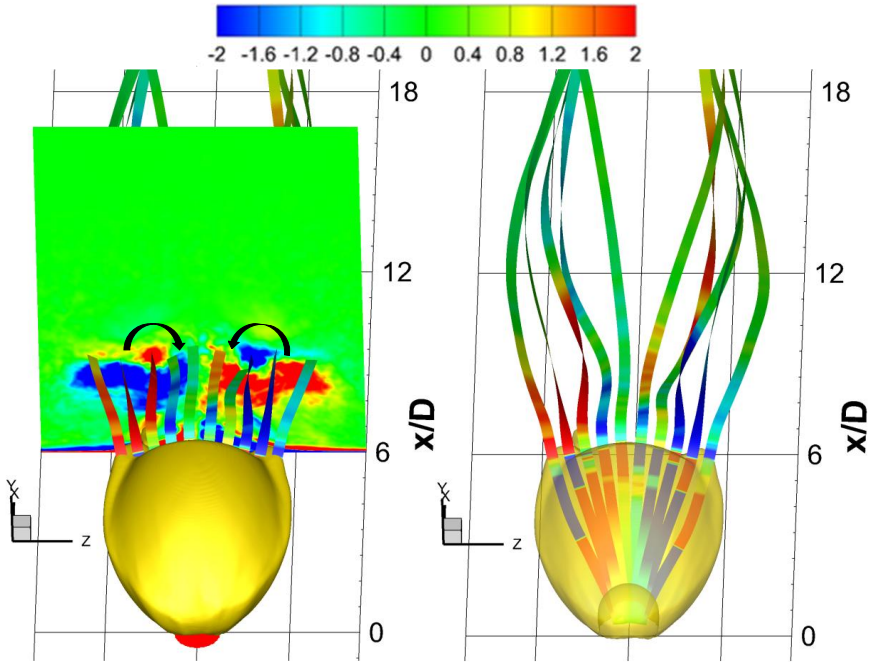

a) stream ribbons penetrating the Mach disk, shown with slice *x/D*=6 (left) and transparent iso-surface of barrel shock (right), colored by streamwise vorticity. Black arrows point out the rotating direction.

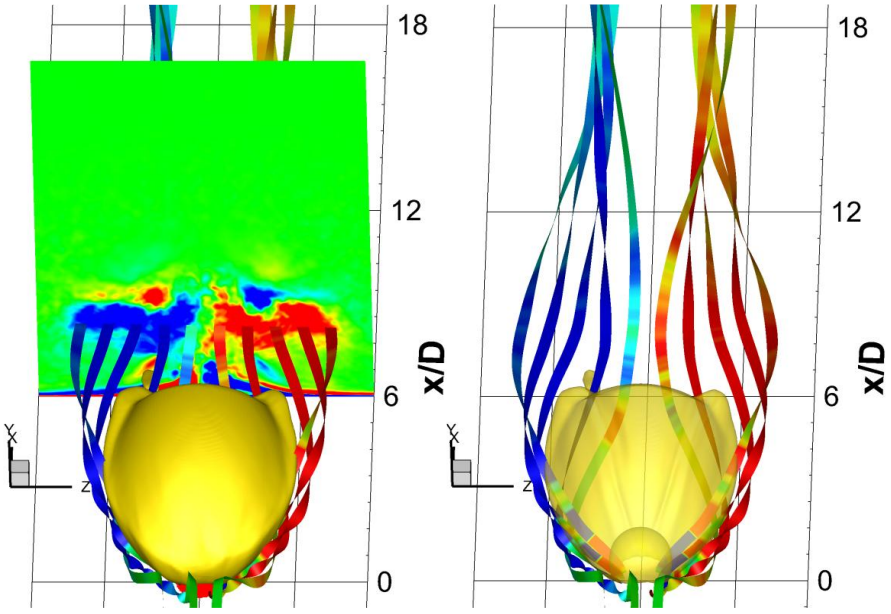

b) stream ribbons running around the jet barrel shock, shown with slice *x/D*=6 (left) and transparent iso-surface of barrel shock (right)

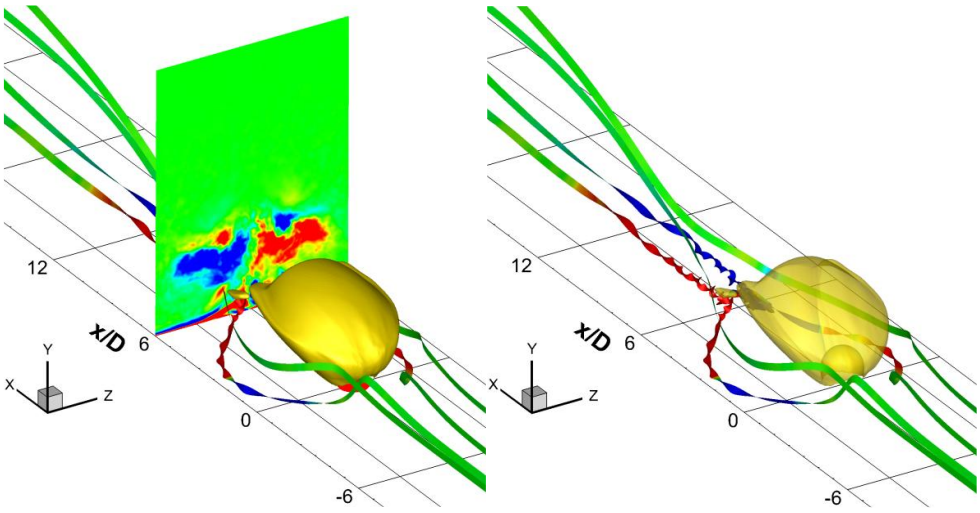

c) lower TCRVs near to the wall surface and the induced TCRVs, shown with slice *x/D*=6 (left) and transparent iso-surface of barrel shock (right)

Fig. 11 Stream ribbons in the jet plume to demonstrate the TCRVs of *J*=5.5, colored by local streamwise vorticity

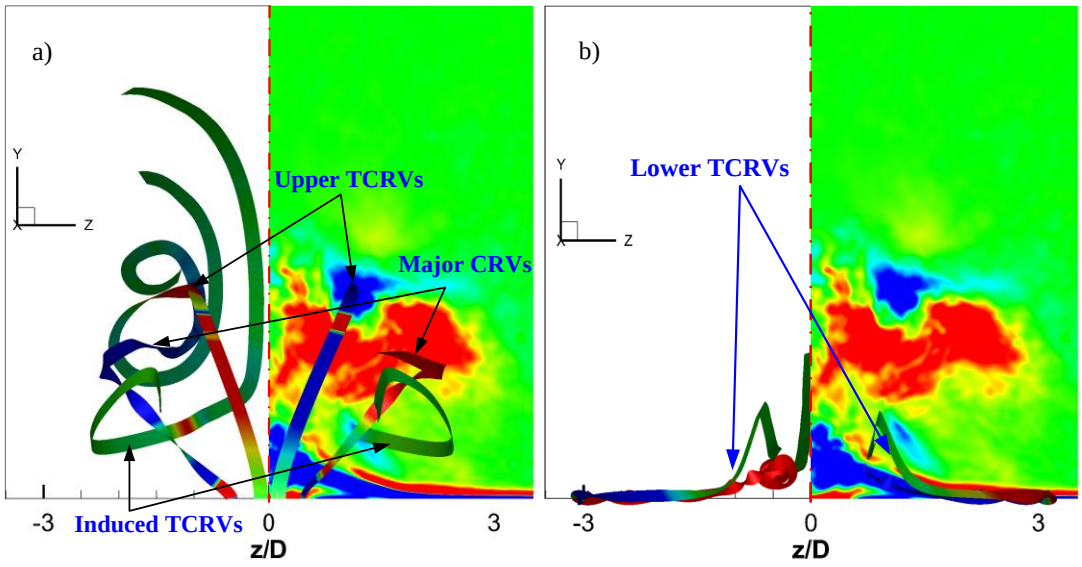

Fig. 12 Stream ribbons of *J*=5.5 to demonstrate the merging process of the upper TCRVs and the induced TCRVs with major CRVs (a) and the motion of lower surface TCRVs (b), colored by local streamwise vorticity, shown with slice *x/D*=6. Same legend as Fig.11 is used.

Fig.12 present front views of stream ribbons which penetrate the upper TCRVs, major TCRVs, induced TCRVs and lower surface TCRVs. The representative stream ribbons also

correspond to the ribbons shown in Fig.11a)-c). Stream ribbons penetrating the major CRVs in the *x/D*=6 slice follow the rotating motion and swirl into the CRV core in the farfield. Stream ribbons penetrating the upper TCRV center are rolled by the major CRVs, merge into major CRVs and arrive at a higher height in the downstream. Stream ribbons penetrating the induced TCRVs are rolled from a position under the major CRVs to a top position due to the effects of major CRVs. An interesting phenomenon is that stream ribbons penetrating the lower surface TCRVs are not rolled into the major CRVs and only get a slight lift near the outlet of the flowfield, which indicates that the lower TCRVs are not affected significantly by major CRVs and only dissipate in the farfield. Generation of major CRVs, induced TCRVs and lower surface TCRVs are not the main point of this study and further analysis of them is omitted here.

Fig.13a)-b) give the Mach number iso-surface superimposed with streamlines 1-4 for *J*=5.5. Streamlines 1 and 3 are colored by local streamwise vorticity and indicate that jet fluid penetrates the upper trailing vortex center. Streamlines 2 and 4 originate from the lateral side of the jet orifice and penetrate the major CRVs. Streamlines 2 and 4 are rolled by the merged CRVs. The voriticities shown on streamlines 1 and 3 are opposite, similar on streamlines 2 and 4, which demonstrates the counter-rotating characteristics. The voriticities on streamlines 1 and 2 are opposite in the same lateral side, which means that the generation mechanism of streamlines 1 and 2 is different. The barrel shock is clearly shown in Fig.13b) by the iso-surface of Mach number 2.8. Fig.13c) gives the barrel shock and streamlines of *J*=1.85 and the flow topology is similar to *J*=5.5. The contrary part is that streamlines from the Mach disk of *J*=1.85 quickly have a sign change in vorticity since the upper trailing vorticity is weak and the upper TCRVs get merged into the major CRVs in a short distance away from the barrel shock.

A summary of the vortical structures in the present study is shown in Fig. 14. This figure shows a schematic of the cross flow section at a location aft of the barrel shock. A system of four pairs of counter-rotating vortices forms ahead of the injector, along the barrel shock wave and immediately downstream of the Mach disk. The pair of upper TCRVs are formed by the interaction of the jet fluid passing through the Mach disk with the crossflow running around the barrel shock. The upper and induced vortex systems trail downstream and finally merge into the major CRVs in the downstream farfield. The lower surface TCRVs are attached to wall and dissipate in the farfield without apparent interaction with major TCRVs.

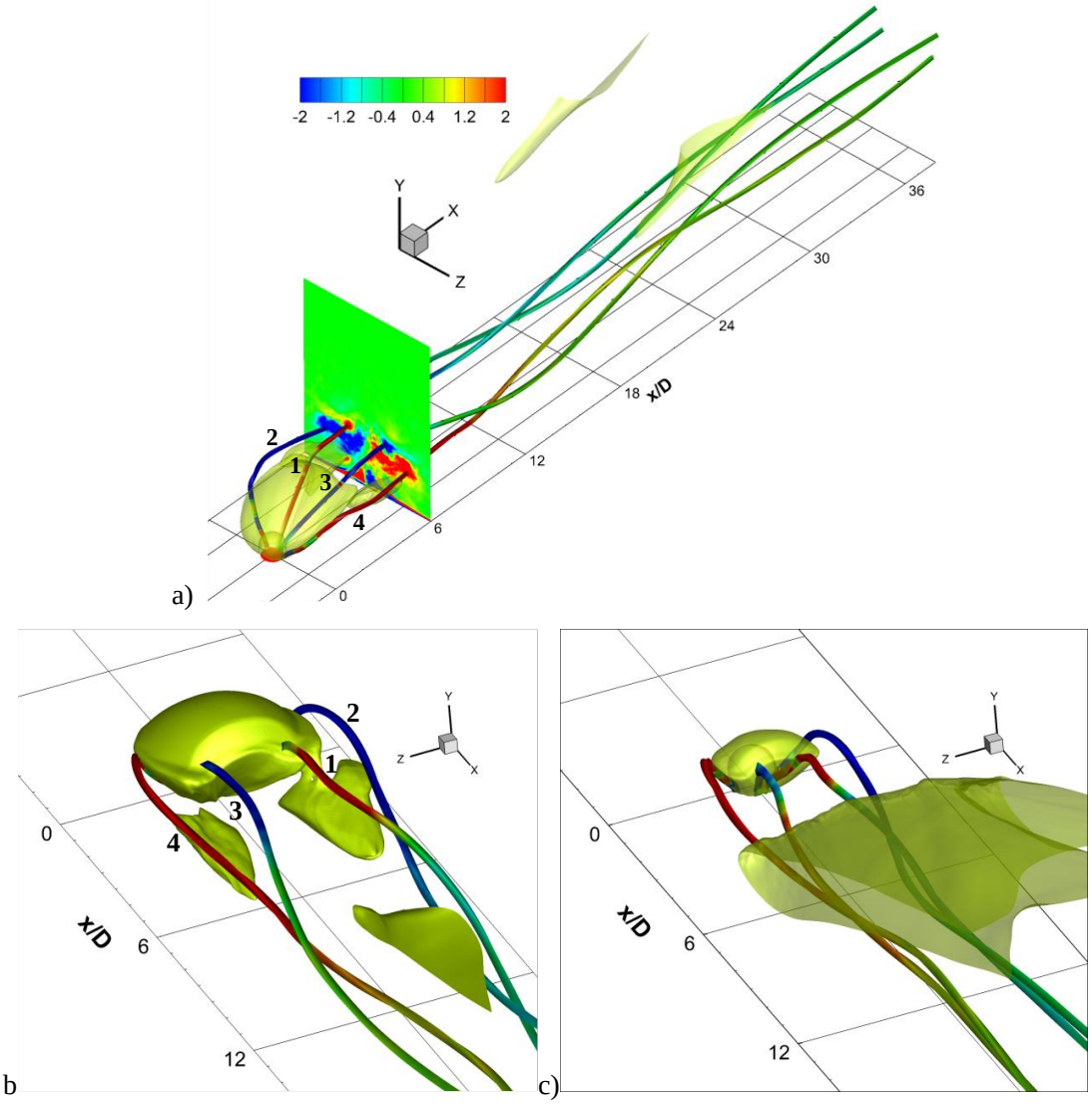

Fig.13 Iso-surface of Mach number (Ma=2.8) demonstrating barrel shock and Mach disk,

combining with streamlines colored by local streamwise vorticity, a) oblique view of the streamlines originating from jet orifice of J=5.5 with iso-surface of Mach number (Ma=2.8), b) Iso-surface of Mach number (Ma=2.8) of J=5.5, c) Iso-surface of Mach number 2.8 is set transparent to show the streamlines of J=1.85.

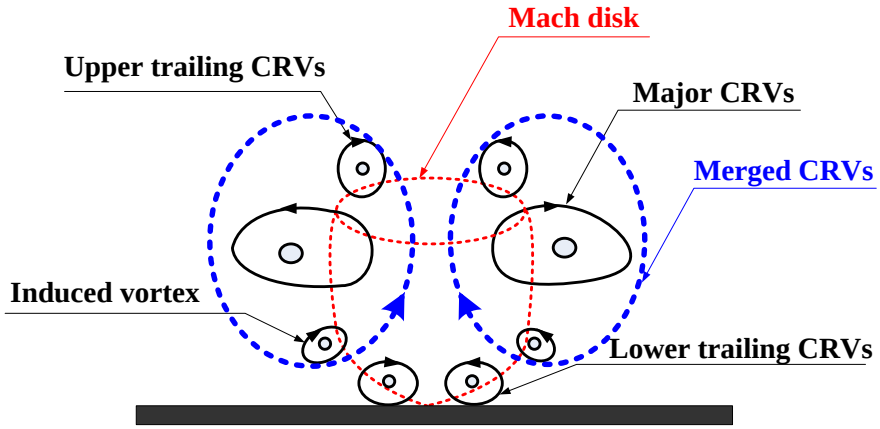

Fig. 14 Schematic of the flow field at a transverse section aft of the barrel shock, abstracted from Fig.8a) and Fig.12d)

3.3 Baroclinic effects on upper TCRVs

Fig.15 demonstrates the local pressure and density contour on the x/D=4.5 slice of the J=5.5 case, which reflects the circumstance streamlines 1-4 running through. As the barrel shock from the wall surface blocks the main stream, it creates the low-pressure and low-density region on the jet leeward side. It is seen that streamlines 1 and 3 are located near to the bounds of the low pressure and density region which means a high pressure and density gradient at this location. As known, the local pressure and density gradient could be related to the vorticity equation, which may be used to further evaluate the vorticity formed in the field. A vector equation for the vorticity could be written as follows,

$$\frac{D\boldsymbol{\omega}}{Dt}=(\boldsymbol{\omega}\cdot\nabla)\mathbf{u}-\boldsymbol{\omega}(\nabla\cdot\mathbf{u})-\frac{\nabla p\times\nabla\rho}{\rho^2}+\nabla\times\left(\frac{\nabla\cdot\tau}{\rho}\right)$$

The third term, $\frac{\nabla p \times \nabla \rho}{\rho^2}$ describes vorticity production via the baroclinic mechanism, which occurs when the density and pressure gradients are misaligned. This term is identically zero in flows where $\rho=\rho(p)$. If the pressure and density gradients are not aligned, the force acting at the center of the pressure induces a torque on the fluid about the center of the mass, creating vorticity. Pressure enters the vorticity equation only through this baroclinic term. It is important to note that vorticity can be generated only by baroclinic torque in the jet plume. All the other terms in the voritcity equation describe the amplification, stretching, bending or diffusion of the vorticity that already exists in the flow. These effects have a limited influence on the vorticity development if they are integrated on the whole field. Thus, rotation of the stream ribbons comes from the complex reorganization of the vorticity that enters the flow from the baroclinic mechanism. A possible flow movement can arise from this vorticity even if hysteresis phenomena exist, depending on the local flow velocity field (note that $\boldsymbol{\omega} = \int \frac{\partial \boldsymbol{\omega}}{\partial t} dt$ and $\Delta t = \Delta s / \|\mathbf{u}\|$).

Physically speaking, the baroclinic term indicates the rate at which the vorticity is generated and pumped into the flow. From this aspect, we could only consider the baroclinic vorticity production to understand the vorticity generation along the streamline ($u_k \left(\partial \boldsymbol{\omega} / \partial x_k\right)$),

$$\frac{\partial \boldsymbol{\omega}}{\partial t} = -\frac{\nabla p \times \nabla \rho}{\rho^2}$$

The streamwise vorticity production via baroclinic torque is obtained as,

$$\frac{\partial \omega_x}{\partial t} = \frac{1}{\rho^2}\left(\frac{\partial \rho}{\partial y}\frac{\partial P}{\partial z} - \frac{\partial \rho}{\partial z}\frac{\partial P}{\partial y}\right)$$

Fig.15c) gives the contour of the local streamwise vorticity production via baroclinic term on *x/D*=4.5 slice, which reflects the circumstance near to the region aft of the Mach disk. It is seen

that streamlines 1 and 3 experience a definitely different region of baraclinic torque from streamlines 2 and 4. Streamlines 1 and 3 penetrate the region with high magnitude of the baroclinic term, while streamlines 2 and 4 penetrate the region with a nearly zero baroclinic term. To clearly show the baroclinic term on the streamlines, Fig.16 is given with iso-surface of Mach number for identifying barrel shock and Mach disk. It is seen that streamlines 2 and 4 gain vorticity production at the windward side of the barrel shock and the vorticity production drops significantly at the lateral of the barrel shock. Streamlines 1 and 3 gain the vorticity production at aft region in the lateral of the Mach disk and the voriticity production is opposite to each other. Recalling Fig.11a), the sign of the vorticity production just corresponds to the rotation direction of the stream ribbons. Streamline 5 shown in Fig.16 is located near to the centerline plane of the jet plume. The vorticity production on streamline 5 approaches zero in the jet barrel shock and after the Mach disk. This indicates that the vorticity on streamlines 1 and 3 is due to the shear effects between the flow penetrating the Mach disk and the high speed flow from the jet lateral side. As streamlines 1-4 convect downstream, the vorticity production decreases to zero, which means there is no further baroclinic torque pumped into the vorticity equation. In the downstream region vorticity stretches or bends and the streamlines only inherit the rotation momentum acquired in the near field region. Streamline 1 is energized by positive vorticity production aft of the Mach disk. But as the upper TCRVs merges into the major CRVs by their suction, the vorticity changes into a negative value, as shown in Fig.13b).

Local baroclinic vorticity production (BVP) on streamlines 1-4 along the x-axis of J=5.5 is shown in Fig 17. As shown in Fig.17a), vorticity production on all the streamlines approaches to zero after x/D=10.0, which means there is no more production and no more rotating energy pumped in the farfield. Fig.17b) provides an enlarged view at x/D<10.0 for Fig.17a). It is clearly seen that

streamlines 1 and 3, streamlines 2 and 4 are basically symmetric, reflecting the symmetric flow topology in the jet field. Streamlines 1 and 3 gain vorticity production at $0.0<x/D<0.8$ which is located in the vicinity of the jet exit. Then at $0.8<x/D<3.0$ they have nearly zero production in the region of the barrel shock ahead of the Mach disk. After the Mach disk, the baroclinic production on streamlines 1 and 3 is obviously increased at $3.0<x/D<6.0$. At $4.0<x/D<4.5$ the vorticity production arrives at peak values corresponding to the highest torque generation in the field at $x/D>4.0$. After $x/D>6.0$ the vorticity production gradually decreases to zero which means that effects of the barrel shock and the Mach disk decay and quench. Streamlines 2 and 4 come from the lateral side of the jet exit with very high baroclinic production near the jet orifice. The vorticity production on streamline 2 drops to a negative value and reaches a peak at $x/D\approx1.0$. At $x/D>1.0$ a rebound occurs and BVP magnitude on streamline 2 becomes slightly positive at $1.5<x/D<5.5$. After $x/D=5.5$ the vorticity production on streamline 2 almost reaches to zero. The same condition happens in streamline 4. The negative production at $0.8<x/D<1.5$ of streamline 2 is opposite to the positive production of streamline 1 at $3.0<x/D<6.0$. Even though there is a slight positive domain for BVP on streamlines at $1.5<x/D<4.0$, the positive increment is slight and only covers 8% of the negative peak at $0.6<x/D<1.5$. Fig.17c)-d) give the streamwise vorticity along streamlines 1 and 2 superimposed with the vorticity production. It is seen that the vorticity magnitude on streamline 2 starts to decrease at $x/D>1.5$ but remains negative at the downstream field, which reflects an opposite rotating direction against streamline 1. The streamwise vorticity on streamline 1 remains positive since the baroclinic term is mainly positive at $1.0<x/D<6.0$. At $x/D>9.0$ the streamwise vorticity decreases to a negative value which corresponds to the merging process with the major CRVs. From the above analysis, it is inferred that the opposite rotating direction of the upper trailing

vorticity against the major CRVs is induced by baroclinic production aft of the Mach disk and disappears downstream by the suction of the major CRVs.

Based on the numerical results and the analysis, it is concluded that the three dimensional jet flow structures lead to different vorticity production and local streamwise rotating directions in the spanwise cross-section. The pair of upper trailing CRVs has a different generation mechanism than the major CRVs that originate from lateral plume. The lateral flow of the Mach disk rotates in an opposite direction against the major CRVs due to the local baroclinic torque. All the trailing CRVs (lower TCRVs excluded) and the major CRVs merge into a pair of major CRVs in the downstream farfield.

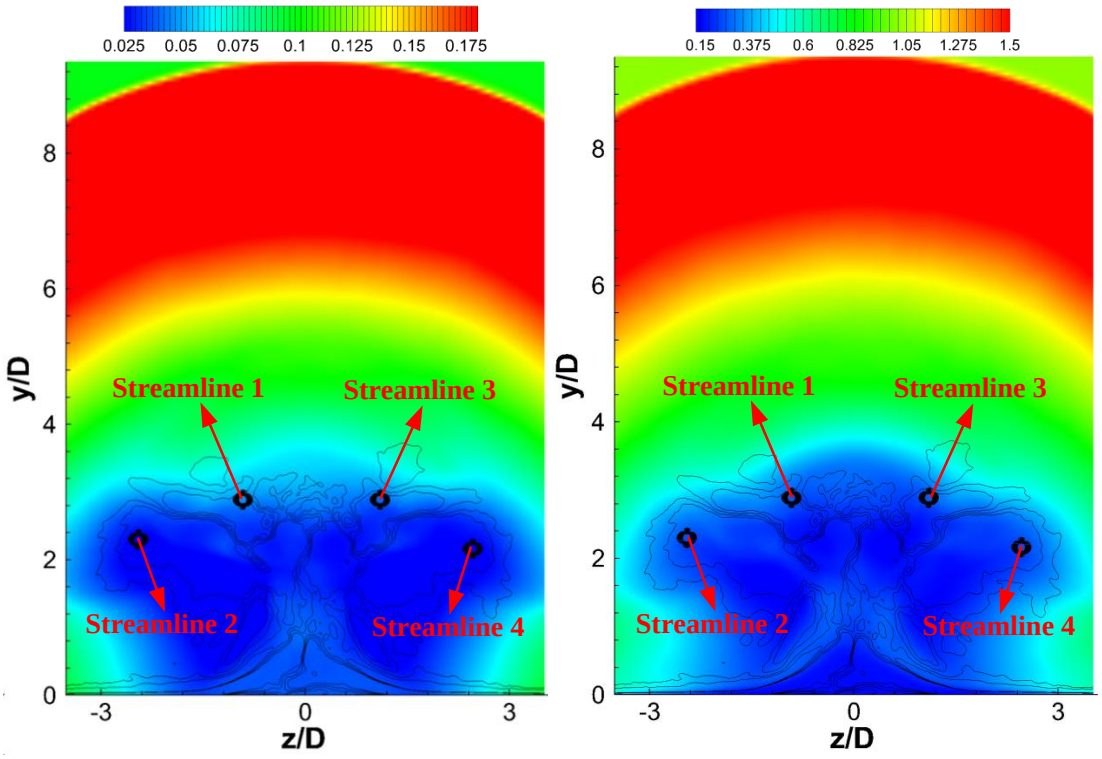

a) pressure contour on slice at x/D=4.5, J=5.5 b) density contour on slice at x/D=4.5, J=5.5

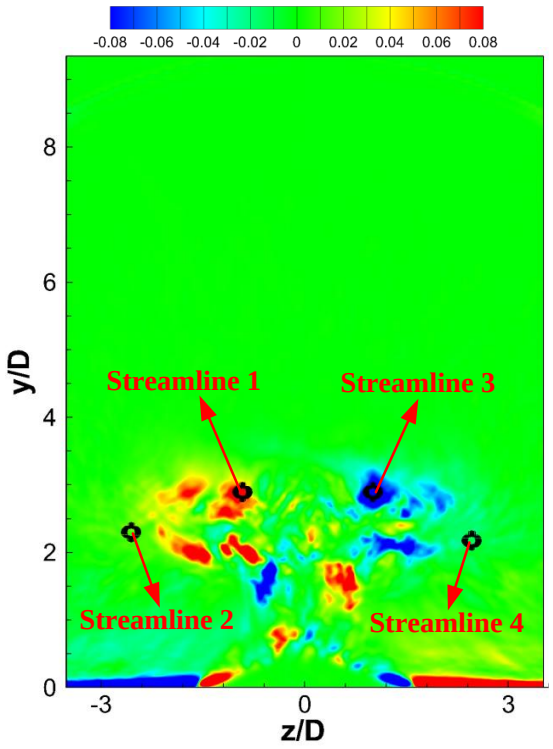

c) contour of baroclinic streamwise vorticity production on slice at x/D=4.5, J=5.5

Fig. 15 Density and pressure contours on slices with different locations aft of the barrel shock, lines of streamwise vorticity distribution are superimposed on Fig.15a)-b).

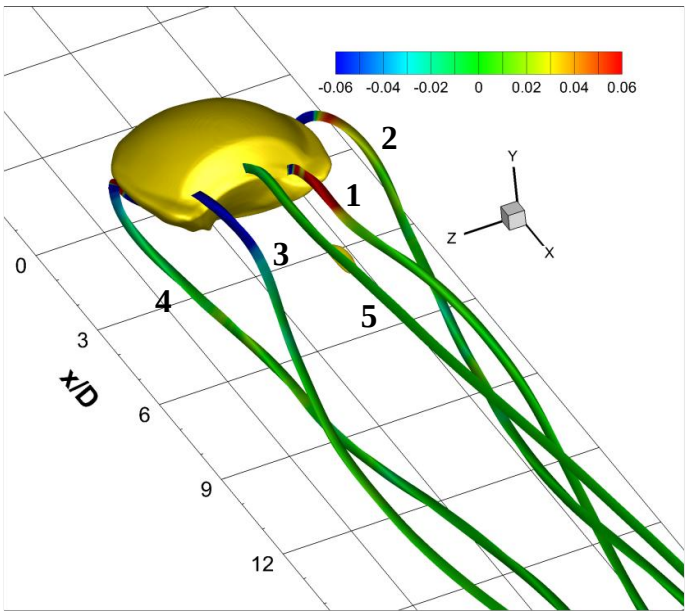

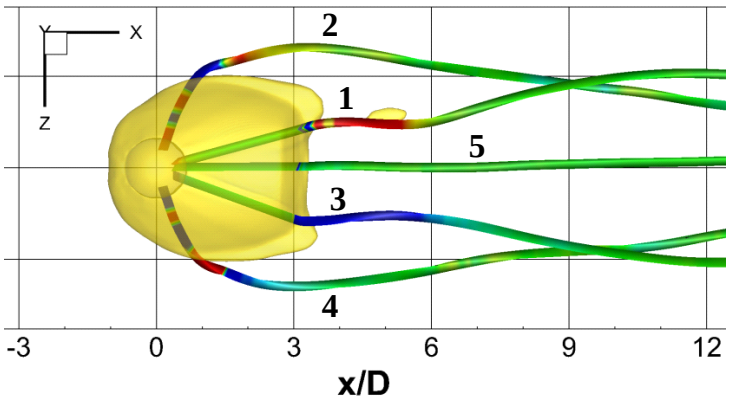

Fig. 16 Iso-surface of Mach number (Ma=3.1) demonstrating barrel shock and Mach disk,

combining with streamlines colored by local baroclinic vorticity production

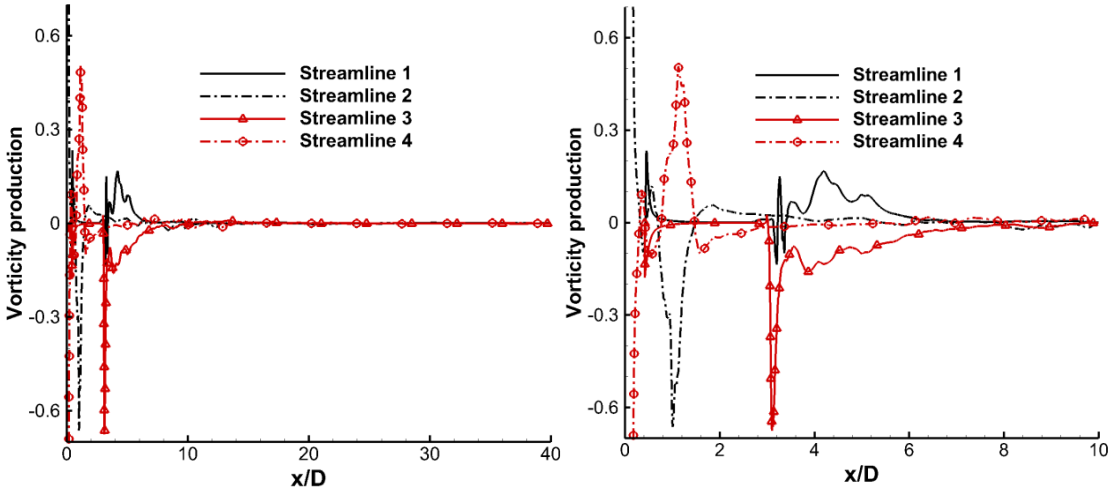

a) *x/D* ranges from 0.0 to 40.0 b) *x/D* ranges from 0.0 to 10.0 for an enlarged view

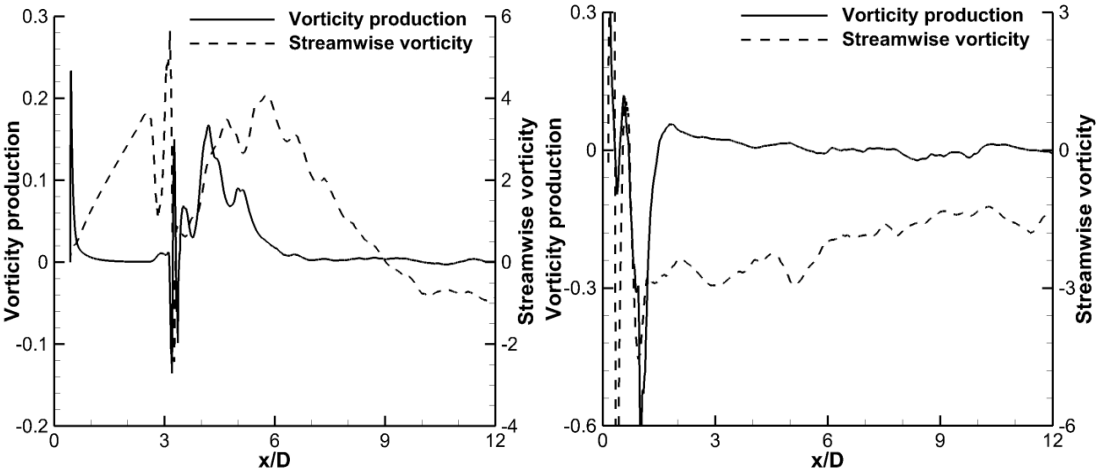

c) vorticity production and streamwise vorticity along streamline 1

d) vorticity production and streamwise vorticity along streamline 2

Fig. 17 Local baroclinic vorticity production on streamlines 1-4 along the x-axis of J=5.5

4. Conclusions

In the present study, direct numerical simulations are conducted to uncover physical aspects of a transverse air jet injected into a supersonic air crossflow at a Mach number of 2.7. Simulations are run for two different jet-to-crossflow momentum flux ratios (J) of 1.85 and 5.5.

The simulations provide the instantaneous and averaged flow features around the transverse jet. The major CRVs form on the lateral side of the jet plume and absorb other induced trailing vorticity. Upper trailing CRVs form above the major CRVs downstream of the jet barrel shock. The upper and induced TCRVs trail downstream and finally merge into the major CRVs in the downstream farfield. The streamline analysis indicates that the upper trailing CRVs are related to the Mach disk where the flow aft of the Mach disk contacts with the high speed flow from the jet lateral side. As the streamlines penetrate the lateral side of Mach disk where the strong shear condition exists, the baroclinic torque induces upper vorticities in the opposite rotating direction against the major CRVs. Downstream of the Mach disk, the baroclinic vorticity production along the streamlines tends to approach zero, which means no more torque is pumped into the farfield and the upper TCRVs are merged into the major CRVs by their suction.

Acknowledgement

Sincere thanks to Professor N. D. Sandham of the University of Southampton for providing the SBLI DNS code and the helpful discussion on data analysis.

Supercomputer time provided by the UK Engineering and Physical Sciences Research Council under the project ‘Thermal and Reactive Flow Simulation on High-End Computers’ (Grant No.

EP/J016381/1) is gratefully acknowledged.

This work is funded by the National Science Foundation of China (grants: 11472305 and 11522222) and outstanding youth fund of National University of Defense Technology.

Appendix A

Assuming that the fluid is inviscid and compressible, we briefly describe the development of a WENO-CU4 (central-upwind 4th order) method for the one-dimensional advection equation in the scalar form

$$\frac{\partial u}{\partial t}+\frac{\partial}{\partial x} f\left(u\right)=0 \tag{A.1}$$

which can be approximated using finite differencing as

$$\frac{d\hat{u}_i}{dt}=-\frac{1}{\Delta x}\left(\hat{f}_{i+1/2}-\hat{f}_{i-1/2}\right), i=0,1...N \tag{A.2}$$

Approximations of the numerical fluxes $\hat{f}_{i\pm1/2}$, are computed from node values f_i. With a typical WENO scheme, $\hat{f}_{i+1/2}$ is reconstructed by a convex combination of the candidate-stencil numerical fluxes $\hat{f}_{k,i+1/2}$ as

$$\hat{f}_{i+1/2}=\sum_{k=0}^{r-1}\omega_k \hat{f}_{k,i+1/2} \tag{A.3}$$

In order to improve the accuracy of the shock-capturing, referring to the method of Hu et al.[22], who introduced the contribution from the centered stencil with the highest possible order-of-accuracy optimal weights, a fourth-order WENO-CU4 scheme, in which where a second-order downwind stencil is added to supplement the two candidate stencils, is constructed. The approximate numerical flux at the cell faces using the downwind candidate stencil is given in Fig. A.1.

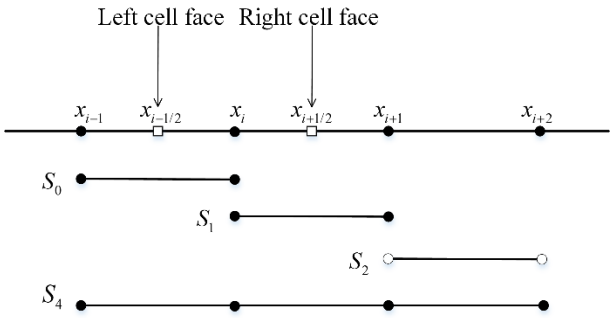

Figure A.1 The computational uniform grid x_i: the 4 point stencil S_4 is composed of three 2-point stencils S_0, S_1, S_2

For simplicity, we only present the interpolation of variables on the left cell face at $x_{i+1/2}$ in one-dimensional space below, since other points are similar.

$$\begin{cases} \hat{f}_{0,i+1/2} = -\dfrac{1}{2} f_{i-1} + \dfrac{3}{2} f_i \\ \hat{f}_{1,i+1/2} = \dfrac{1}{2} f_i + \dfrac{1}{2} f_{i+1} \\ \hat{f}_{2,i+1/2} = \dfrac{3}{2} f_{i+1} - \dfrac{1}{2} f_{i+2} \end{cases} \tag{A.4}$$

The smoothness indicators are given as

$$\begin{cases} \beta_0 = \left(-f_{i-1} + f_i\right)^2 \\ \beta_1 = \left(-f_i + f_{i+1}\right)^2 \\ \beta_2 = \left(-f_{i+1} + f_{i+2}\right)^2 \end{cases} \tag{A.5}$$

The fourth-order central linear interpolation on the stencil S_4 as shown in Fig. 1 is given by

$$\hat{f}_{4,i+1/2} = -\frac{1}{12} f_{i-1} + \frac{7}{12} f_i + \frac{7}{12} f_{i+1} - \frac{1}{12} f_{i+2} \tag{A.6}$$

The fourth-order central linear interpolation is a linear combination of the three second-order interpolations in Eqs. (A.4) and (A.5).

$$\hat{f}_{4,i+1/2} = \sum_{k=0}^{2} d_k \hat{f}_{k,i+1/2} \tag{A.7}$$

Then the optimal weights d_k are computed as

$$d_0 = \frac{1}{6}, d_1 = \frac{2}{3}, d_2 = \frac{1}{6}$$

Following Hu et al.[22], the fourth-order nonlinear interpolation can be constructed by introducing

nonlinear weights,

$$\hat{f}_{i+1/2} = \sum_{k=0}^{2} \omega_k \hat{f}_{k,i+1/2}$$

The nonlinear weights ω_k are given by

$$\omega_k = \frac{\alpha_k}{\sum_{k=0}^{2} \alpha_k}, \alpha_k = d_k \left(C + \frac{\tau_4}{\beta_k + \varepsilon} \right), k = 0,1,2$$

where τ_4 denotes the reference smoothness indicator. The parameter *C* is introduced to improve the performance of the smoothness indicator in smooth flow regions. The smoothness indicator for the downwind stencil utilizes the four-point stencil S_4 for the fourth-order central linear interpolation.

$$\beta_4 = \frac{1}{36}\left(-2f_{i-1} - 3f_i + 6f_{i+1} - f_{i+2}\right)^2 + \frac{13}{12}\left(f_{i-1} - 2f_i + f_{i+1}\right)^2 + \frac{781}{720}\left(-f_{i-1} + 3f_i - 3f_{i+1} + f_{i+2}\right)^2$$

Using a Taylor expansion for β_i, we have

$$\begin{cases} \beta_0 = f'^2\Delta x^2 + \frac{1}{4} f''^2\Delta x^4 - ff''\Delta x^3 + \frac{1}{3} ff'''\Delta x^4 + O\left(\Delta x^5\right) \\ \beta_1 = f'^2\Delta x^2 + \frac{1}{4} f''^2\Delta x^4 + ff''\Delta x^3 + \frac{1}{3} ff'''\Delta x^4 + O\left(\Delta x^5\right) \\ \beta_2 = f'^2\Delta x^2 + \frac{9}{4} f''^2\Delta x^4 + 3ff''\Delta x^3 + \frac{7}{3} ff'''\Delta x^4 + O\left(\Delta x^5\right) \\ \beta_4 = f'^2\Delta x^2 + \frac{13}{12} f''^2\Delta x^4 + O\left(\Delta x^5\right) \end{cases}$$

Finally the reference smoothness indicator τ_4 is defined as

$$\tau_4 = \beta_4 - \left(\frac{\beta_0 + \beta_1}{2} \right) \tag{A.8}$$

So that τ_4 is $O\left(\Delta x^4\right)$. Note that the smoothness indicator β_3 for the third reconstruction stencil is abandoned and replaced by the smoothness indicator for the optimal four-point interpolation stencil.

Reference

[1] Karagozian A R. Transverse jets and their control. Progress in Energy Combustion Science, 2010, 36 (5):531-553

[2] Mahesh K. The interaction of jets with crossflow. Annual Review Fluid Mechanics, 2013, 45:379-407

[3] Ben-Yakar A, Mungal G M, Hanson R K. Time evolution and mixing characteristics of hydrogen and ethylene transverse jets in supersonic crossflows. Physics of Fluids, 2006, 18:26-101

[4] Gamba M, Mungal M G. Ignition, flame structure and near-wall burning in transverse hydrogen jets in supersonic crossflow. Journal of Fluid Mechanics, 2015, 780:226-273

[5] Viti V, Neel R, Schetz J A. Detailed Flow Physics of the Supersonic Jet Interaction Flow Field. Physics of Fluids, 2009, 21 (4):046101

[6] Santiago J G, Dutton J C. Velocity measurements of a jet injected into a supersonic crossflow. Journal of Propulsion and Power, 1997, 13 (2):264-273

[7] Everett D E, Woodmansee M A, Dutton J C, Morris M J. Wall Pressure Measurements for a Sonic Jet Injected Transversely Into a Supersonic Crossflow. Journal of Propulsion and Power, 1998, 14 (6):861–886

[8] Portz R, Segal C. Penetration of Gaseous Jets In Supersonic Flows. AIAA Journal, 2006, 44 (10):2426-2429

[9] Gruber M R, Nejad A S, Chen T H, Dutton J C. Large structure convection velocity measurements in compressible transverse injection flowfields. Experiments in Fluids, 1997, 22:397-407

[10] Sun M B, Zhang S P, Zhao Y H, Zhao Y X, Liang J H. Experimental investigation on transverse jet penetration into a supersonic turbulent crossflow. Science China,Technological Sciences, 2013, 56 (8):1989–1998

[11] Kawai S, Lele S K. Large-Eddy Simulation of Jet Mixing in Supersonic Crossflows. AIAA Journal, 2010, 48 (9):2063-2083

[12] Rana Z A, Thornber B, Drikakis D. Transverse jet injection into a supersonic turbulent cross-flow. Physics of Fluids, 2011, 23 (046103):1-22

[13] Won S-H, Jeung I-S, Parent B, Choi J-Y. Numerical Investigation of Transverse Hydrogen Jet into Supersonic Crossflow Using Detached-Eddy Simulation. AIAA Journal, 2010, 48 (6):1047-1058

[14] Chai X, Iyer P S, Mahesh K. Numerical study of high speed jets in crossflow. Journal of Fluid Mechanics, 2015, 785:152-188

[15] Wang H B, Wang Z G, Sun M B, Qin N. Hybrid Reynolds-averaged Navier-Stokes/large-eddy simulation of jet mixing in a supersonic crossflow. Science China,Technological Sciences, 2013, 56 (6):1435-1448

[16] Zhang Y J, Liu W D, Sun M B. Effect of microramp on transverse jet in supersonic crossflow. AIAA Journal, 2016, 54 (12):4041-4044

[17] Sandham N D, Schülein E, Wagner A, Willems S, Steelant J. Transitional shock-wave/boundary-layer interactions in hypersonic flow. Journal of Fluid Mechanics, 2014, 752:349-382

[18] Xie Z T, Castro I P. Efficient generation of inflow conditions for large-eddy simulation of street-scale flows. Flow Turbulence and Combustion, 2008, 81:449-470

[19] Sandham N D, Johnstone R, Jacobs C T. Surface-sampled simulations of turbulent flow at high Reynolds number. International Journal of Numerical Methods in Fluids, 2017:1-13

[20] Sandham N D, Li Q, Yee H C. Entropy splitting for high-order numercial simulation of compressible turbulence. Journal of Computational Physics, 2002, 178:307-322

[21] Yee H C, Sandham N D, Djomehri M J. Low-dissipative high-order shock-capturing methods using characteristic-based filters. Journal of Computational Physics, 1999, 150:199-238

[22] Hu X Y, Wang Q, Adams N A. An adaptive central-upwind weighted essentially non-oscillatory scheme. Journal of Computational Physics, 2010, 229:8952-8965

[23] Ducros F, Ferrand V, Nicoud F, Weber C, Darracq D, Gacherieu C, Poinsot T. Large-Eddy Simulation of the Shock/Turbulence Interaction. Journal of Computational Physics, 1999, 152:517-549

[24] Touber E. Unsteadiness in shock wave boundary layer interactions. PhD thesis, University of Southampton, 2010

[25] Wang B, Sandham N D, Hu Z, W Liu. Numerical study of oblique shock-wave/boundary-layer interaction considering sidewall effect. Journal of Fluid Mechanics, 2015, 767:526-561

[26] Touber E, Sandham N D. Large-eddy simulation of low-frequency unsteadiness in a turbulent shock-induced separation bubble. Theoretical and Computational Fluid Dynamics, 2009, 23:79-107

[27] Schlatter P, Orlu R. Assessment of direct numerical simulation data of turbulent boundary layers. Journal of Fluid Mechanics, 2010, 659:116-126

[28] Kolář V. Compressibility Effect in Vortex Identification. AIAA Journal, 2009, 47 (2):473-475

[29] Morkovin M V. Effects of compressibility on turbulent flows, in In Mecanique de la Turbulence (ed. A. Favre) CNRS, pp. 367-380, 1962

[30] Duan L, Beekman I, Martin M P. Direct numerical simulation of hypersonic turbulent boundary layers. Part 3. Effect of Mach number. Journal of Fluid Mechanics, 2011, 672:245-267

[31] White F M. Viscous Fluid Flow. McGraw Hill, 3rd edition, 2006